Supplement of Atmos. Chem. Phys., 26, 15853–15875, 2026
https://doi.org/10.5194/acp-26-15853-2026-supplement
© Author(s) 2026. CC BY 4.0 License.



Atmospheric Chemistry and Physics
Open Access
EGU

Supplement of

Drivers of biogenic secondary organic aerosol from the past to the future

Yang Shi et al.

Correspondence to: Yang Shi (yang.shi@pnnl.gov) and Colette L. Heald (colette.heald@env.ethz.ch)

The copyright of individual parts of the supplement might differ from the article licence.

Text S1. Discussion regarding photolysis

We turn off the photolysis of SOA in the lowest volatility bin to mimic the photo-recalcitrant fraction as observed in previous laboratory studies (O'Brien and Kroll, 2019; Sun and Smith, 2024; Zawadowicz et al., 2020). This is a simplification based entirely in convenience and computational cost (specifying a photo-recalcitrant fraction for each SOA species would add 92 advected tracers, and 92 non-advected tracers to the configuration).

The simplification may overemphasize the isomerization and $RO_2 + RO_2$ reactions, which form SOA solely in the lowest volatility bin (Table 2, part 1 and part 2). To understand this uncertainty, we conducted a 1-year experiment with NEW_slow chemical configuration in PD conditions while retaining photolysis loss for the lowest volatility bin. This experiment represents a condition where all SOA volatility bins are subject to the same photolysis rate (i.e. no recalcitrant fraction is considered, and OA photolysis loss is excessive). In this sensitivity experiment, SOA formed through isomerization and $RO_2 + RO_2$ reaction accounts for 38% and 2.6% of the total MTERP + OH SOA. This is slightly lower than our current estimates (44% and 3.3%, respectively) from NEW_slow in PD (Figure 2b), however isomerization still dominates. This implies that the isomerization contribution to SOA in PI and F are also slightly overpredicted (Figure 9b), and the SOA increase from PD to F due to isomerization has a minor high bias (Figure 10a).

Text S2. Experimental settings for PI, PD, and F

Our experiments for the pre-industrial (PI), present-day (PD), and future (F) conditions utilize sea surface temperature (SST), sea ice, CO_2 concentrations, anthropogenic and natural emissions of aerosols and reactive gases, and land use data representing 1850, 2010, and 2100 conditions, respectively. SST and sea ice for PI and PD originate from Hadley Centre sea ice and

SST dataset (Hurrell et al., 2008). PI uses data for 1850, which is constructed by SST and sea ice climatology from 1870 to 1889. PD uses 2010 climatology, which is averaged from 2005 to 2015. The future SST and sea ice are generated from a fully coupled CESM2 experiment that was conducted under SSP5-8.5 trajectory and uses data from 2100 single year. The CO2 concentrations for PI and PD conditions are taken from Meinshausen et al. (2017), with PI represented by the 1850 climatology (averaged from 1845 to 1855) and PD represented by the 2010 climatology (averaged from 2006 to 2014). Future CO_2 concentrations follow the SSP5 pathway from Riahi et al. (2017), using the projected values for the year 2100. Anthropogenic emissions of aerosols and reactive gases for PI and PD originate from the Community Emissions Data System (Hoesly et al., 2018), while the biomass burning emissions for PI and PD are constructed by van Marle et al. (2017). The future anthropogenic and biomass burning emissions are projected following the SSP5 pathway (Gidden et al., 2019). PI, PD, and F experiments are conducted with climatological emissions for 1850 (averaged from 1850 to 1859), 2010 (averaged from 2006 to 2014), and 2100 (averaged from 2091 to 2100), respectively. Emissions of biogenic volatile organic compounds (BVOCs) are calculated online through the Model of Emissions of Gases and Aerosols from Nature (MEGAN2) parameterization (see Section 2.1). The BVOC emissions are impacted by vegetation types determined by land use. The land use conditions for PI, PD, and F are taken from the dataset of Land-Use Harmonization 2 project (Hurtt et al., 2020) for single year 1850, 2010, and 2100, respectively. All the prescribed input data are in one-year length and used cyclically throughout the model integration. We note that the temporal treatments for these input datasets differ, due to the availability of existing input files. The influence on results is likely small because data from within a decade tend to be more consistent than those from different climate conditions.

Text S3. Calculation of fRO_2

In the BASE experiment, the OH oxidation of ISOP, MTERP, and BCARY only produces one RO_2 species, respectively. fRO_2 for a specific RO_2 reaction is simply calculated as its vertically integrated reaction rate divided by the sum of the vertically integrated reaction rates of all RO_2 reactions. To determine the globally averaged fRO_2 shown in Figures 2 and 9, we weight the gridded fRO_2 by the RO_2 concentrations at each grid cell.

In our modified chemistry (i.e., the NEW experiments), the OH oxidation of MTERP produces two RO_2 species, MTERP-RO_2-1 and MTERP-RO_2-2, with branching ratios of 0.78 and 0.22, respectively. The two RO_2 undergo identical chemistry, except that only MTERP-RO_2-2 can isomerize. To determine the averaged fRO_2, we calculate fRO_2 for the two RO_2 species separately and weight them by their branching ratios. This method ensures reaction fates of each RO_2 species do not exceed its branching ratio (e.g., the isomerization fate does not exceed 22%). ISOP oxidation produces six RO_2 species through two-step reactions (Schwantes et al., 2020). Four isoprene hydroxy alkyl radical isomers (i.e., ISOPC1T, ISOPC1C, ISOPC4T, and ISOPC4C) are formed through the first-step oxidation:

ISOP + OH → 0.315*ISOPC1T + 0.315*ISOPC1C + 0.111*ISOPC4T + 0.259*ISOPC4C

$$\text{Rate constant} = 2.7 \times 10^{-11} e^{(390/T)} \ [\text{cm}^3\ \text{molecule}^{-1}\ \text{s}^{-1}] \quad (1)$$

Then, O_2 radicals attach to these isomers, forming six ISOP-RO_2 species:

ISOPC1T + O2 → ISOPB1O2 Rate constant = 7.5×10^{-13} [s^{-1}] (2)

ISOPC1T + O2 → ISOPED1O2 Rate constant = 3.6×10^{-13} [s^{-1}] (3)

ISOPC1C + O2 → ISOPB1O2 Rate constant = 7.5×10^{-13} [s^{-1}] (4)

ISOPC1C + O2 → ISOPZD1O2 Rate constant = 1.4×10^{-13} [s^{-1}] (5)

ISOPC4T + O2 → ISOPB4O2 Rate constant = 6.5×10^{-13} [s^{-1}] (6)

ISOPC4T + O2 → ISOPED4O2 Rate constant = 4.9×10^{-13} [s^{-1}] (7)

ISOPC4C + O2 → ISOPB4O2 Rate constant = 6.5×10^{-13} [s^{-1}] (8)

ISOPC4C + O2 → ISOPZD4O2 Rate constant = 2.1×10^{-13} [s^{-1}] (9)

Each alkyl radical isomer forms two types of ISOP-RO_2 at different reaction rates. Therefore, to determine the branching ratio of each RO_2 species (BR_{RO_2}), we scale the stoichiometric coefficients of the alkyl radical isomers (R1) with the corresponding reaction rate constants (R2-9):

$$BR_{ISOPB1O2} = 0.315 * \frac{7.5 \times 10^{-13}}{7.5 \times 10^{-13} + 3.6 \times 10^{-13}} + 0.315 * \frac{7.5 \times 10^{-13}}{7.5 \times 10^{-13} + 1.4 \times 10^{-13}}$$

$$= 0.478$$

$$BR_{ISOPB4O2} = 0.111 * \frac{6.5 \times 10^{-13}}{6.5 \times 10^{-13} + 4.9 \times 10^{-13}} + 0.259 * \frac{6.5 \times 10^{-13}}{6.5 \times 10^{-13} + 2.1 \times 10^{-13}}$$

$$= 0.259$$

$$BR_{ISOPED1O2} = 0.315 * \frac{3.6 \times 10^{-13}}{7.5 \times 10^{-13} + 3.6 \times 10^{-13}} = 0.102$$

$$BR_{ISOPED4O2} = 0.111 * \frac{4.9 \times 10^{-13}}{6.5 \times 10^{-13} + 4.9 \times 10^{-13}} = 0.048$$

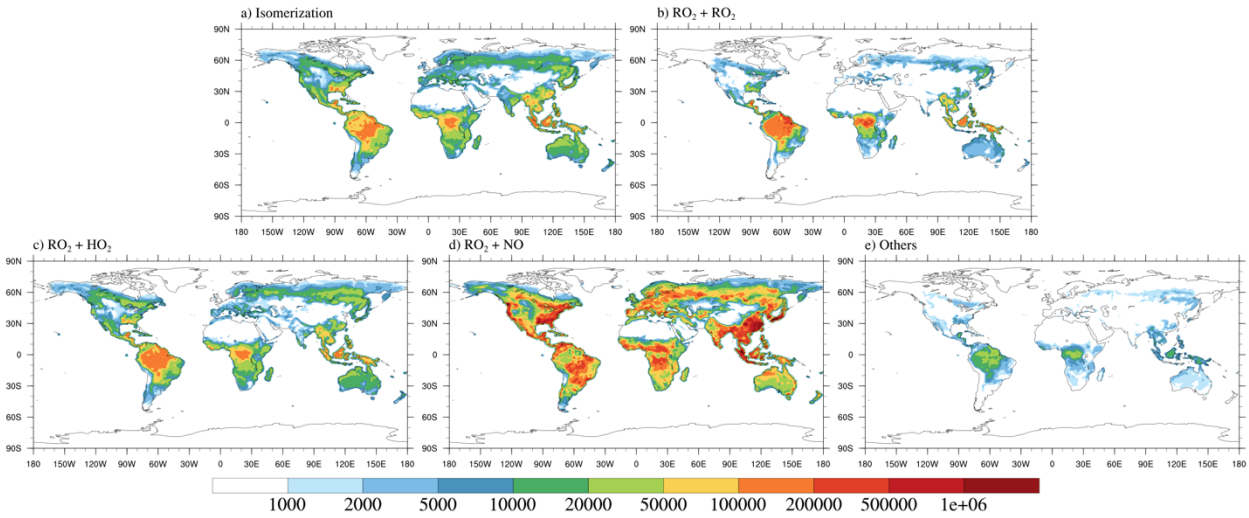
$$BR_{ISOPZD1O2} = 0.315 * \frac{1.4 \times 10^{-13}}{7.5 \times 10^{-13} + 1.4 \times 10^{-13}} = 0.050$$

$$BR_{ISOPZD4O2} = 0.259 * \frac{2.1 \times 10^{-13}}{6.5 \times 10^{-13} + 2.1 \times 10^{-13}} = 0.063$$

Similar to MTERP-RO_2, the averaged fRO_2 for ISOP-RO_2 in the NEW experiments are calculated as the fRO_2 of individual RO_2 species weighted by the corresponding branching ratios. To determine the globally averaged fRO_2 shown in Figures 2 and 9, we weight the gridded fRO_2 by the RO_2 concentrations at each grid cell.

Table S1. SOA burden and loss budget for PI_PDB, PI, PD, F, and F_PDB. Unit for the loss budget is Tg/yr. The numbers in parentheses are lifetime that corresponds with each loss term (unit: day).

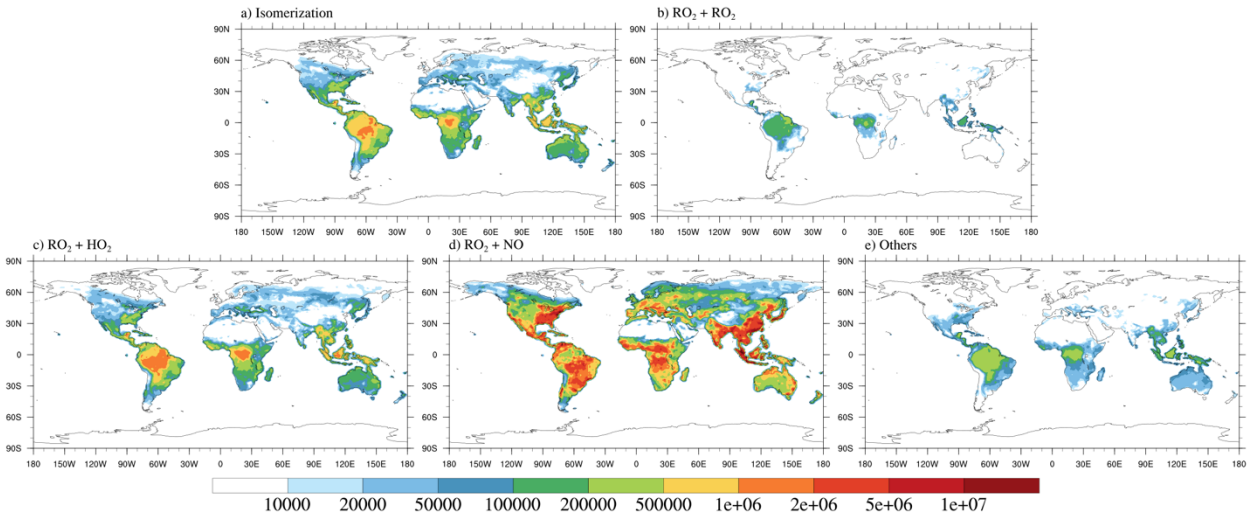
	Burden (Tg)	Photolytic loss	Wet deposition	Dry deposition
ISOP SOA				
PI_PDB	0.28	14.6 (7.0)	9.4 (10.9)	0.6 (170.3)
PI	0.32	16.7 (7.0)	11.6 (10.1)	0.7 (166.9)
PD	0.20	10.2 (7.2)	8.9 (8.2)	0.7 (104.3)
F	0.23	11.5 (7.3)	9.9 (8.5)	0.6 (139.9)
F_PDB	0.14	6.6 (7.7)	5.8 (8.8)	0.4 (127.8)
MTERP SOA				
PI_PDB	0.21	4.6 (16.7)	13.8 (5.6)	2.0 (38.3)
PI	0.24	5.0 (17.5)	15.7 (5.6)	2.0 (43.8)
PD	0.20	3.6 (20.3)	14.4 (5.1)	2.0 (36.5)
F	0.60	9.1 (24.1)	35.9 (6.1)	4.4 (49.8)
F_PDB	0.20	3.0 (24.3)	13.0 (5.6)	1.8 (40.6)
Total SOA				
PI_PDB	0.49	19.2 (9.3)	23.3 (7.7)	2.7 (66.2)
PI	0.56	21.6 (9.5)	27.2 (7.5)	2.8 (73.0)
PD	0.40	13.8 (10.6)	23.3 (6.3)	2.7 (54.1)
F	0.83	20.6 (14.7)	45.8 (6.6)	5.0 (60.6)
F_PDB	0.34	9.6 (12.9)	18.8 (6.6)	2.2 (56.4)



100

101 **Figure S1.** Annually averaged MTERP-RO_2 reaction rates at the surface from NEW_slow. The
102 reaction rates are the sum of the rates of the corresponding reactions of all RO_2 species, with no
103 weight applied. The RO_2 + RO_2 reactions include those between MTERP-RO_2 and ISOP-RO_2,
104 IEPOXOO, MTERP-RO_2 itself, BCARY-RO_2, and later generations of terpene RO_2 (Table 2,
105 part 2), while the reactions with NO_3, CH_3O_2, and CH_3CO_3 are included in "Others". Unit:
106 molecular/cm^3/s.

107



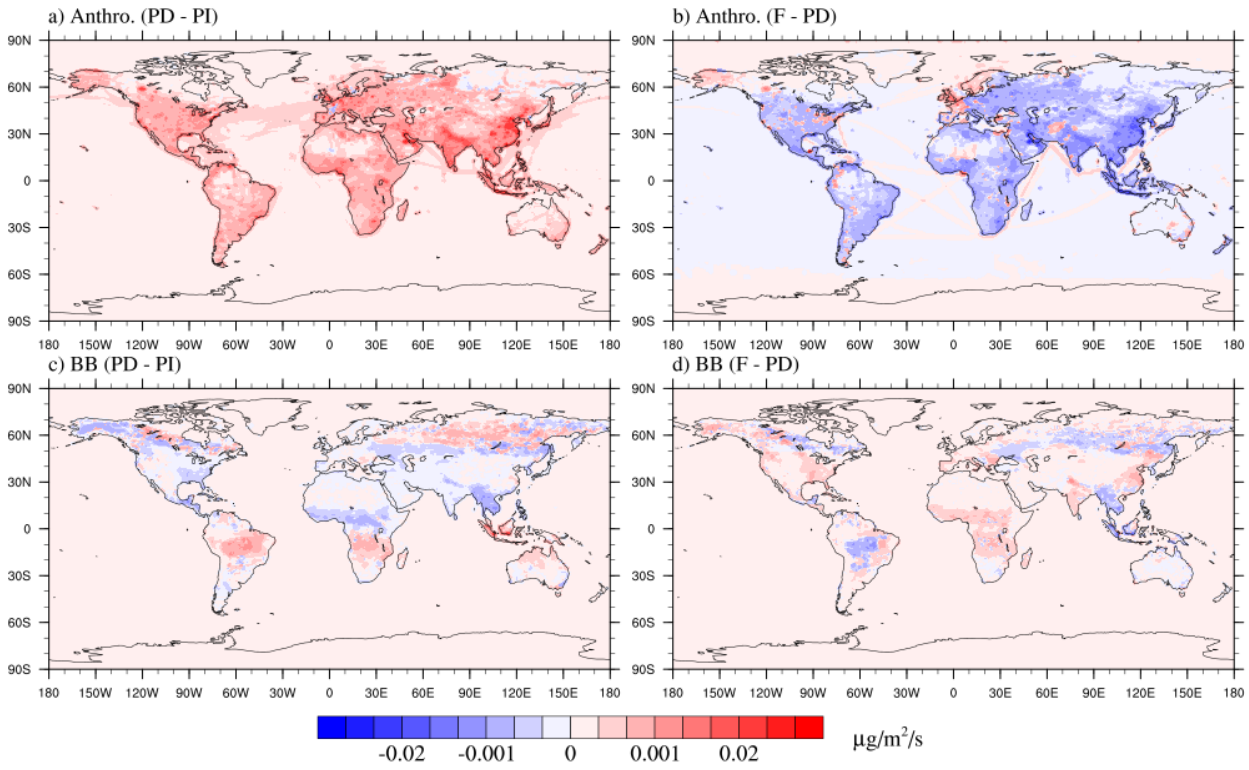
108

109 **Figure S2.** Same as Figure S1, except for ISOP-RO_2 reactions. The RO_2+RO_2 reactions include

110 ISOP-RO_2 + MTERP-RO_2 and ISOP-RO_2 + BCARY-RO_2 reactions (Table 2, part 2), while

111 "Others" include ISOP-RO_2 decomposition and the reactions with CH_3O_2 and CH_3CO_3.

112



113

114 **Figure S3.** Historical (left panel) and future (right panel) changes of toluene emissions from

115 anthropogenic (Anthro.) and biomass burning (BB) sources. The other anthropogenic and biomass

116 burning VOC species follow the same trends.

117

Reference

Gidden, M. J., Riahi, K., Smith, S. J., Fujimori, S., Luderer, G., Kriegler, E., van Vuuren, D. P., van den Berg, M., Feng, L., Klein, D., Calvin, K., Doelman, J. C., Frank, S., Fricko, O., Harmsen, M., Hasegawa, T., Havlik, P., Hilaire, J., Hoesly, R., Horing, J., Popp, A., Stehfest, E., and Takahashi, K.: Global emissions pathways under different socioeconomic scenarios for use in CMIP6: a dataset of harmonized emissions trajectories through the end of the century, Geoscientific Model Development, 12, 1443–1475, https://doi.org/10.5194/gmd-12-1443-2019, 2019.

Hoesly, R. M., Smith, S. J., Feng, L., Klimont, Z., Janssens-Maenhout, G., Pitkanen, T., Seibert, J. J., Vu, L., Andres, R. J., Bolt, R. M., Bond, T. C., Dawidowski, L., Kholod, N., Kurokawa, J., Li, M., Liu, L., Lu, Z., Moura, M. C. P., O'Rourke, P. R., and Zhang, Q.: Historical (1750–2014) anthropogenic emissions of reactive gases and aerosols from the Community Emissions Data System (CEDS), Geoscientific Model Development, 11, 369–408, https://doi.org/10.5194/gmd-11-369-2018, 2018.

Hurrell, J. W., Hack, J. J., Shea, D., Caron, J. M., and Rosinski, J.: A New Sea Surface Temperature and Sea Ice Boundary Dataset for the Community Atmosphere Model, https://doi.org/10.1175/2008JCLI2292.1, 2008.

Hurtt, G. C., Chini, L., Sahajpal, R., Frolking, S., Bodirsky, B. L., Calvin, K., Doelman, J. C., Fisk, J., Fujimori, S., Klein Goldewijk, K., Hasegawa, T., Havlik, P., Heinimann, A., Humpenöder, F., Jungclaus, J., Kaplan, J. O., Kennedy, J., Krisztin, T., Lawrence, D., Lawrence, P., Ma, L., Mertz, O., Pongratz, J., Popp, A., Poulter, B., Riahi, K., Shevliakova, E., Stehfest, E., Thornton, P., Tubiello, F. N., van Vuuren, D. P., and Zhang, X.: Harmonization of global land use change and management for the period 850–2100 (LUH2) for CMIP6, Geoscientific Model Development, 13, 5425–5464, https://doi.org/10.5194/gmd-13-5425-2020, 2020.

van Marle, M. J. E., Kloster, S., Magi, B. I., Marlon, J. R., Daniau, A.-L., Field, R. D., Arneth, A., Forrest, M., Hantson, S., Kehrwald, N. M., Knorr, W., Lasslop, G., Li, F., Mangeon, S., Yue, C., Kaiser, J. W., and van der Werf, G. R.: Historic global biomass burning emissions for CMIP6 (BB4CMIP) based on merging satellite observations with proxies and fire models (1750–2015), Geoscientific Model Development, 10, 3329–3357, https://doi.org/10.5194/gmd-10-3329-2017, 2017.

Meinshausen, M., Vogel, E., Nauels, A., Lorbacher, K., Meinshausen, N., Etheridge, D. M., Fraser, P. J., Montzka, S. A., Rayner, P. J., Trudinger, C. M., Krummel, P. B., Beyerle, U., Canadell, J. G., Daniel, J. S., Enting, I. G., Law, R. M., Lunder, C. R., O'Doherty, S., Prinn, R. G., Reimann, S., Rubino, M., Velders, G. J. M., Vollmer, M. K., Wang, R. H. J., and Weiss, R.: Historical greenhouse gas concentrations for climate modelling (CMIP6), Geoscientific Model Development, 10, 2057–2116, https://doi.org/10.5194/gmd-10-2057-2017, 2017.

O'Brien, R. E. and Kroll, J. H.: Photolytic Aging of Secondary Organic Aerosol: Evidence for a Substantial Photo-Recalcitrant Fraction, J. Phys. Chem. Lett., 10, 4003–4009, https://doi.org/10.1021/acs.jpclett.9b01417, 2019.

Riahi, K., van Vuuren, D. P., Kriegler, E., Edmonds, J., O'Neill, B. C., Fujimori, S., Bauer, N., Calvin, K., Dellink, R., Fricko, O., Lutz, W., Popp, A., Cuaresma, J. C., Kc, S., Leimbach, M., Jiang, L., Kram, T., Rao, S., Emmerling, J., Ebi, K., Hasegawa, T., Havlik, P., Humpenöder, F., Da Silva, L. A., Smith, S., Stehfest, E., Bosetti, V., Eom, J., Gernaat, D., Masui, T., Rogelj, J., Strefler, J., Drouet, L., Krey, V., Luderer, G., Harmsen, M., Takahashi, K., Baumstark, L., Doelman, J. C., Kainuma, M., Klimont, Z., Marangoni, G., Lotze-Campen, H., Obersteiner, M., Tabeau, A., and Tavoni, M.: The Shared Socioeconomic Pathways and their energy, land use, and greenhouse gas emissions implications: An overview, Global Environmental Change, 42, 153–168, https://doi.org/10.1016/j.gloenvcha.2016.05.009, 2017.

Schwantes, R. H., Emmons, L. K., Orlando, J. J., Barth, M. C., Tyndall, G. S., Hall, S. R., Ullmann, K., St. Clair, J. M., Blake, D. R., Wisthaler, A., and Bui, T. P. V.: Comprehensive isoprene and terpene gas-phase chemistry improves simulated surface ozone in the southeastern US, Atmospheric Chemistry and Physics, 20, 3739–3776, https://doi.org/10.5194/acp-20-3739-2020, 2020.

Sun, M. and Smith, G. D.: Photolytic Mass Loss of Humic Substances Measured with a Quartz Crystal Microbalance, ACS Earth Space Chem., https://doi.org/10.1021/acsearthspacechem.4c00134, 2024.

Zawadowicz, M. A., Lee, B. H., Shrivastava, M., Zelenyuk, A., Zaveri, R. A., Flynn, C., Thornton, J. A., and Shilling, J. E.: Photolysis Controls Atmospheric Budgets of Biogenic Secondary Organic Aerosol, Environ. Sci. Technol., 54, 3861–3870, https://doi.org/10.1021/acs.est.9b07051, 2020.